Research Square

Preprints are preliminary reports that have not undergone peer review.
They should not be considered conclusive, used to inform clinical practice,
or referenced by the media as validated information.

Gravitational wave radiation from periodic orbits around a noncommutative-inspired black hole surrounded by quintessence

Shavkat Karshiboev
Samarqand State Pedagogical Institute
Shakhnoza Gafforova
Samarqand State Pedagogical Institute
Yulduz Mardanova
Navoi State University of Mining and Technologies
Jamshid Parmanov
Samarkand State Architectural and Civil-Engineering Institute
Axror Eshtemirov
Shakhrisabz State Pedagogical Institute
Abubakir Shermatov
shermatov.abubakir98@gmail.com

Institute of Fundamental and Applied Research, National Research University TIIAME

Research Article

Keywords: noncommutative geometry, quintessence, periodic orbits, gravitational waves, zoom-whirl orbits, effective potential, ISCO, test particle dynamics, extreme mass-ratio inspiral

Posted Date: July 27th, 2026

DOI: https://doi.org/10.21203/rs.3.rs-10291743/v1

License: This work is licensed under a Creative Commons Attribution 4.0 International License.
Read Full License

Additional Declarations: No competing interests reported.

Gravitational wave radiation from periodic orbits around a noncommutative-inspired black hole surrounded by quintessence

Shavkat Karshiboev[a], Shakhnoza Gafforova[a], Yulduz Mardanova[b], Jamshid Parmanov[c], Axror Eshtemirov[d], Abubakir Shermatov[e,f,g]

[a]*Samarqand State Pedagogical Institute, Spitamen Shokh Street 166, Samarkand 140100, Uzbekistan*
[b]*Navoi State University of Mining and Technologies, Galaba Shokh Street 27, Navoi, Uzbekistan*
[c]*Lecturer at the Department of Social and Natural Sciences, Samarkand State University of Architecture and Civil Engineering*
[d]*Shakhrisabz State Pedagogical Institute, Shakhrisabz Street 10, Samarkand 140100, Uzbekistan*
[e]*Institute of Fundamental and Applied Research, National Research University TIIAME, Kori Niyoziy 39, Tashkent 100000, Uzbekistan*
[f]*University of Tashkent for Applied Sciences, Str. Gavhar 1, Tashkent 100149, Uzbekistan*
[g]*Tashkent State Technical University, Tashkent 100095, Uzbekistan*

Abstract

We study the gravitational-wave (GW) emission from periodic orbits of a massive test particle around a noncommutative-inspired black hole surrounded by a quintessence (NCiBHSQ) field with equation-of-state parameter $\omega_q = -2/3$. The geometry is governed by two parameters: the quintessence field strength parameter p and the noncommutative parameter Θ, which deform the spacetime in complementary radial domains. Using the Hamiltonian formalism, we derive the equations of motion and analyze the effective potential, the specific energy and angular momentum of circular orbits, and the innermost stable and innermost bound circular orbits (ISCO and IBCO). We classify timelike periodic orbits by the zoom-whirl taxonomy with three topological integers (z, w, v) and compute representative GW waveforms in both the plus (h_+) and cross $(h_\times)$ polarizations within the kludge approximation. We find that the linear term restricts the existence of bound periodic orbits to a narrow band of p, and that both p and Θ leave measurable imprints on the orbital energies and on the emitted waveforms: increasing Θ shifts the orbital structure inward, while a more negative p raises the energy of periodic orbits. The characteristic strains fall in the millihertz band accessible to space-based detectors such as LISA, suggesting that future GW missions could probe or constrain noncommutative and quintessence corrections in the strong-field regime.

Keywords: noncommutative geometry, quintessence, periodic orbits, gravitational waves, zoom-whirl orbits, effective potential, ISCO, test particle dynamics, extreme mass-ratio inspiral

1. Introduction

The advent of gravitational-wave (GW) astronomy, opened by the detection of GWs by LIGO and Virgo in 2015 [1, 2], has provided a new observational window onto the most energetic processes in the Universe and onto the strong-field regime of gravity. Together with the first horizon-scale images of supermassive BHs by the Event Horizon Telescope [3], these achievements allow theoretical models of accretion and orbital dynamics near compact objects to be confronted with observations. Among the trajectories of test particles around BHs, periodic orbits are of particular importance: they govern the long-term stability of bound systems, they encode the structure of the underlying spacetime, and every generic bound orbit can be regarded as a small deformation of a periodic one [4, 5].

Stellar-mass compact objects or neutron stars are frequently found on tight orbits around supermassive BHs, forming extreme mass-ratio inspirals (EMRIs), which are among the primary targets of future space-based detectors such as LISA [6, 7]. Because the energy radiated per orbit is a tiny fraction of the total energy of the system, the inspiral proceeds adiabatically and the orbital dynamics of the smaller body is well approximated by a sequence of periodic orbits [8]. Analyzing the corresponding GW signals therefore yields precise information about the orbital motion and the gravitational field of the central object.

A systematic classification of periodic orbits for massive particles was introduced by Levin and Perez-Giz [4]: every closed orbit around a BH is labelled by three topological integers describing its zoom, whirl, and vertex structure. Under this taxonomy, periodic orbits and their GW emission have been studied in a wide range of spacetimes, including Schwarzschild, Kerr, and naked-singularity geometries [9–11], charged BHs, hairy BHs, and many modified-gravity backgrounds [12–14]. These orbits exhibit characteristic zoom-whirl behaviour, with the particle returning to its initial location after a finite time.

In parallel, two physically motivated modifications of the

Email addresses: q.shavkat5453@gmail.com (Shavkat Karshiboev), shaxnoza20192015@gmail.com (Shakhnoza Gafforova), shaxrizodayulduz@gmail.com (Yulduz Mardanova), jamshidparmanov1987@gmail.com (Jamshid Parmanov), axroreshtimerov1982@gmail.com (Axror Eshtemirov), shermatov.abubakir98@gmail.com (Abubakir Shermatov)

Schwarzschild background have attracted considerable attention. The first is the quintessence field [15], which models the large-scale effect of a surrounding dark-energy-like fluid characterized by an equation-of-state parameter ω_q and a field strength parameter p. The second is the noncommutative correction to the central source [16–18], motivated by the noncommutative structure of spacetime coordinates, which replaces the point-like mass by a smeared, regular mass distribution controlled by a noncommutative parameter Θ with a characteristic length scale $\sqrt{\Theta}$. While p governs the long-range, large-radius modification of the geometry, Θ encodes the short-distance smearing of the mass near the horizon, so that the two corrections act in complementary radial domains.

In this work, we combine these two effects and study a static, spherically symmetric NCiBHSQ with $\omega_q = -2/3$, for which contribution becomes linear in the radial coordinate. We investigate the timelike periodic geodesic orbits of a massive test particle in this background and compute the associated GW radiation. We map the parameter space of energy and angular momentum that supports bound motion, identify the characteristic orbital radii (ISCO and IBCO), classify the periodic orbits by the integer triplet (z, w, v), and evaluate the plus and cross GW polarizations within the kludge approximation [19–21]. We show how the quintessence parameter p and the noncommutative parameter Θ modify both the orbital structure and the emitted waveforms.

The paper is organized as follows. In Section 2, we introduce the NCiBHSQ metric and discuss its horizon structure. In Section 3, we derive the equations of motion of a test particle using the Hamiltonian formalism. Section 4 analyzes the effective potential, the specific energy and angular momentum of circular orbits, and the ISCO and IBCO radii. In Section 5, we classify the periodic orbits and tabulate their energies. Section 6 presents the GW radiation emitted by these periodic orbits. Finally, Section 7 summarizes our conclusions. Throughout the paper, we use the metric signature $(-,+,+,+)$ and units in which $G = c = 1$, unless stated otherwise.

2. The NCiBHSQ metric

We consider a static, spherically symmetric spacetime that combines two physically distinct effects: the quintessence field surrounding the BH, characterized by the field strength parameter p, and a noncommutative correction to the central source, described by the noncommutative parameter Θ. The line element reads

$$ds^2 = -f(r)\,dt^2 + \frac{dr^2}{f(r)} + r^2\left(d\theta^2 + \sin^2\theta\, d\phi^2\right). \tag{1}$$

In the commutative Kiselev spacetime, the metric function is [15]

$$f(r) = 1 - \frac{2M}{r} - \frac{p}{r^{3\omega_q+1}}, \tag{2}$$

where M is the BH mass and ω_q is the equation-of-state parameter of the surrounding quintessence field. The parameter p measures how strongly the quintessence field modifies the Schwarzschild geometry, and in the limit $p \to 0$ the spacetime reduces to the Schwarzschild solution.

The noncommutative correction is introduced by replacing the point-like source with a smeared mass distribution, motivated by the noncommutative structure of spacetime coordinates $[x^a, x^b] = i\,\theta^{ab}$, where θ^{ab} is an antisymmetric tensor and the scalar parameter Θ sets the smearing length scale $\sqrt{\Theta}$ [17]. The constant mass M is thus replaced by a radial mass function obtained from the smeared density profile,

$$\rho_\Theta(r) = \frac{M\sqrt{\Theta}}{r^{3/2}\left(r^2 + \pi\Theta\right)^2}, \tag{3}$$

which yields, for small Θ, the leading-order mass $M(r,\Theta) \simeq M - \frac{4M}{\sqrt{\pi}\,r}\sqrt{\Theta}$. Inserting this smeared mass into the Kiselev geometry gives the metric function

$$f(r) = 1 - \frac{2M}{r} + \frac{8M}{\sqrt{\pi}\,r^2}\sqrt{\Theta} - \frac{p}{r^{3\omega_q+1}}. \tag{4}$$

In this work we focus on the quintessence case

$$\omega_q = -\frac{2}{3}, \tag{5}$$

for which the Kiselev contribution becomes linear in r and Eq. (4) reduces to

$$f(r) = 1 - \frac{2M}{r} + \frac{8M}{\sqrt{\pi}\,r^2}\sqrt{\Theta} - pr. \tag{6}$$

This expression clearly separates the two corrections. The term $\propto \sqrt{\Theta}/r^2$ is controlled by the noncommutative parameter and mainly affects the near-horizon region, while the term $-pr$ is controlled by the quintessence field strength parameter and becomes more relevant as the radial distance increases. The limiting cases provide useful consistency checks: for $\Theta \to 0$ one recovers the ordinary Kiselev BH with $\omega_q = -2/3$; for $p \to 0$ the noncommutative-inspired Schwarzschild solution is recovered; and for $\Theta \to 0$ and $p \to 0$ one obtains the standard Schwarzschild spacetime. Throughout, we set $M = 1$.

2.1. Horizon structure

The horizons are the positive roots of $f(r) = 0$, and the relevant event horizon is the outer root. Since the two correction terms have different radial dependences, they modify the horizon position through different mechanisms. The boundary between BH and no-BH configurations follows from the degenerate-horizon conditions $f(r) = 0$ and $f'(r) = 0$. We find that the existence of an event horizon is restricted by the combined values of Θ and p: as p becomes more negative, the parameter domain admitting BH solutions becomes narrower. Motivated by this behaviour, we adopt the intervals $\Theta \in (0, 0.04)$ and $p \in (-0.10, 0)$ in what follows, which keep the solutions inside the physically relevant BH region.

Figure 1 shows the radial profile of $f(r)$ for different values of the field strength parameter p at fixed $\Theta = 0.01$. Since $p < 0$, the field strength enters as $-pr = |p|r$; hence, more negative values of p raise the metric function in the intermediate

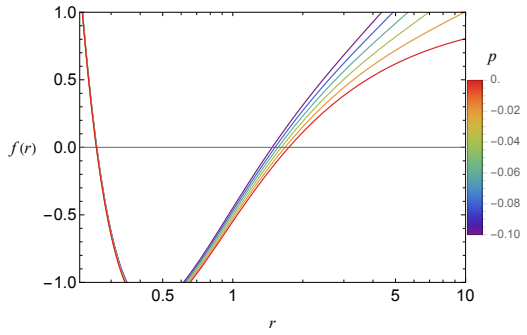


Figure 1: Radial profile of the metric function $f(r)$ for different values of the quintessence field strength parameter p at fixed $\Theta = 0.01$.

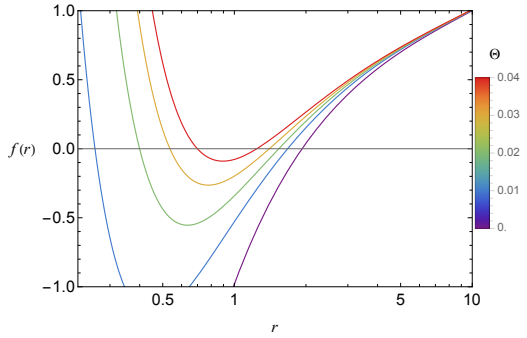


Figure 2: Radial profile of the metric function $f(r)$ for different values of the noncommutative parameter Θ at fixed $p = -0.05$.

and outer regions and move the outer horizon toward smaller radii. Figure 2 shows the effect of the noncommutative parameter Θ at fixed $p = -0.05$. In contrast to the p term, the noncommutative correction is proportional to $\sqrt{\Theta}/r^2$ and is therefore concentrated in the inner region: increasing Θ changes the near-horizon profile more strongly than the outer part of the spacetime, reflecting the smearing of the central mass source.

3. Test-particle dynamics

We consider the motion of a massive test particle in the NCiBHSQ. The dynamics follows from the geodesic Lagrangian $2L = g_{\mu\nu}\dot{x}^\mu\dot{x}^\nu$, where the overdot denotes differentiation with respect to the proper time τ. The stationarity and spherical symmetry of the metric (1) give two conserved quantities associated with the Killing vectors $\xi^\mu_{(t)} = (1,0,0,0)$ and $\xi^\mu_{(\phi)} = (0,0,0,1)$ [22], namely the specific energy $\mathcal{E}$ and the specific azimuthal angular momentum $\mathcal{L}$,

$$\mathcal{E} = f(r)\,\dot{t}, \qquad \mathcal{L} = r^2\sin^2\theta\,\dot{\phi}. \tag{7}$$

Adopting the Hamiltonian formalism $\mathcal{H} = \frac{1}{2}g^{\mu\nu}p_\mu p_\nu$ [23], the cyclic nature of t and ϕ confirms the conservation of $p_t = -\mathcal{E}$ and $p_\phi = \mathcal{L}$. Using Hamilton's equations $\dot{x}^\mu = \partial\mathcal{H}/\partial p_\mu$ and $\dot{p}_\mu = -\partial\mathcal{H}/\partial x^\mu$, and restricting the motion to the equatorial plane $\theta = \pi/2$ with $\dot{\theta} = 0$, the normalization condition $g_{\mu\nu}\dot{x}^\mu\dot{x}^\nu = -1$ for timelike geodesics gives the radial equation

$$\dot{r}^2 = \mathcal{E}^2 - f(r)\left(1 + \frac{\mathcal{L}^2}{r^2}\right). \tag{8}$$

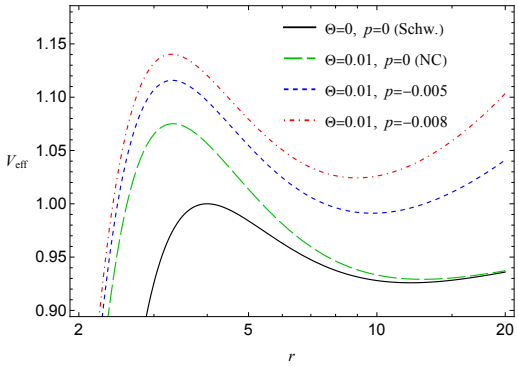


Figure 3: Effective potential $V_{\rm eff}$ for different values of the quintessence field strength parameter p at fixed $\Theta = 0.01$ and $\mathcal{L} = 4M$.

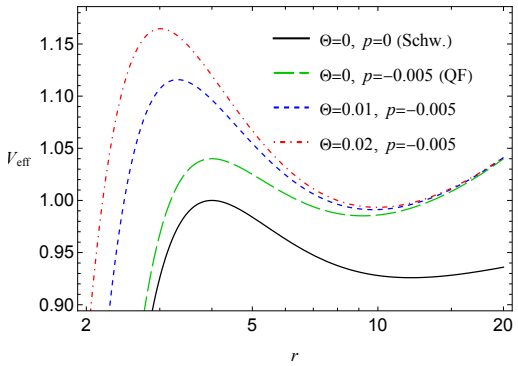


Figure 4: Effective potential $V_{\rm eff}$ for different values of the noncommutative parameter Θ at fixed $p = -0.05$ and $\mathcal{L} = 4M$.

This can be written in the form $\dot{r}^2 + V_{\rm eff}(r) = \mathcal{E}^2$, with the effective potential

$$V_{\rm eff}(r) = f(r)\left(1 + \frac{\mathcal{L}^2}{r^2}\right). \tag{9}$$

4. Effective potential and circular orbits

Using the metric function (6), the effective potential becomes

$$V_{\rm eff}(r) = \left(1 - \frac{2M}{r} + \frac{8M}{\sqrt{\pi}\,r^2}\sqrt{\Theta} - pr\right)\left(1 + \frac{\mathcal{L}^2}{r^2}\right). \tag{10}$$

As expected for an asymptotically flat background, the term proportional to $\sqrt{\Theta}/r^2$ dominates the inner region, while the linear term $-pr$ modifies a wider radial domain. Figures 3 and 4 show the separate influence of the two corrections. In Fig. 3, since $p < 0$, the term $-pr$ gives a positive contribution to the metric function, so decreasing p shifts $V_{\rm eff}$ upward and raises its local minimum, indicating that the quintessence field increases the specific energy required for circular motion and weakens the binding of the corresponding orbits. In Fig. 4, the Θ-dependent correction is concentrated in the inner region: increasing Θ raises the inner part of the potential and makes the local peak more pronounced, reflecting the short-distance modification of the central mass distribution.

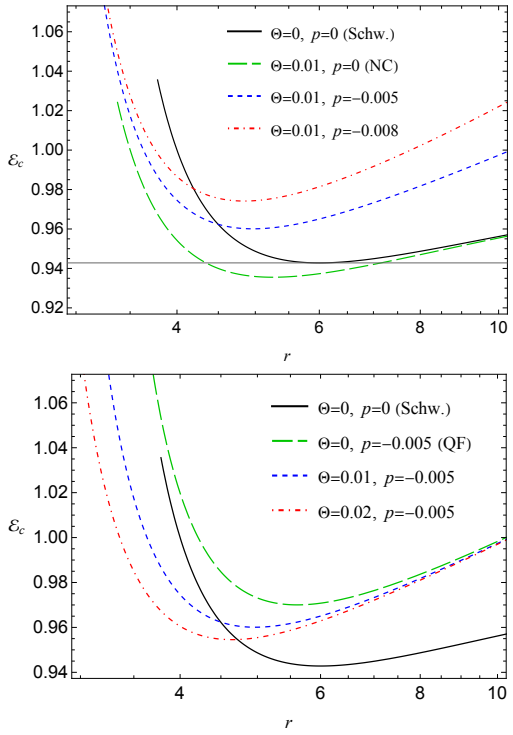


Figure 5: Specific energy $\mathcal{E}_c$ for circular orbits as a function of r/M. Top: different values of p at fixed $\Theta = 0.01$. Bottom: different values of Θ at fixed $p = -0.05$.

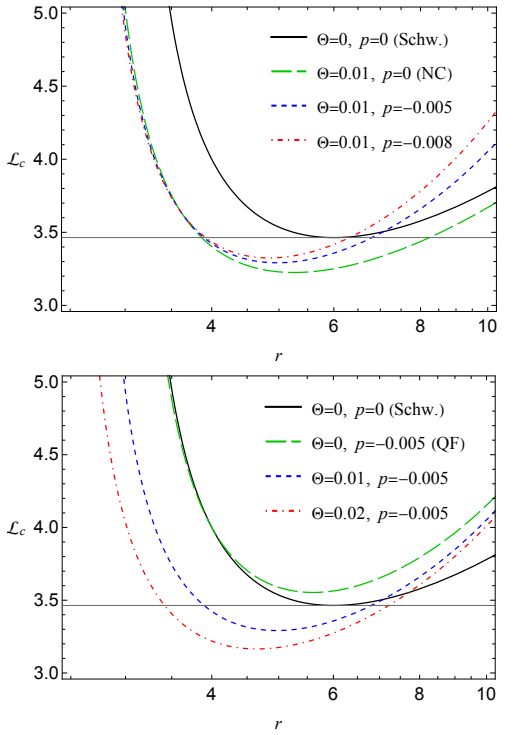


Figure 6: Specific angular momentum $\mathcal{L}_c$ for circular orbits as a function of r/M. Top: different values of p at fixed $\Theta = 0.01$. Bottom: different values of Θ at fixed $p = -0.05$.

4.1. Circular motion

Circular orbits satisfy $V_{\rm eff}(r) = \mathcal{E}^2$ and $dV_{\rm eff}/dr = 0$. For a static, spherically symmetric spacetime these conditions yield the specific energy and angular momentum of a massive particle on a circular orbit,

$$\mathcal{E}_c^2 = \frac{2f^2(r)}{2f(r) - rf'(r)} = \frac{2\left(8\sqrt{\Theta}M - \sqrt{\pi}r(2M + r(pr-1))\right)^2}{\pi r^3(6M + r(pr-2)) - 32\sqrt{\pi}\sqrt{\Theta}Mr^2} \tag{11}$$

$$\mathcal{L}_c^2 = \frac{r^3 f'(r)}{2f(r) - rf'(r)} = \frac{r^2\left(16\sqrt{\Theta}M + \sqrt{\pi}r\left(pr^2 - 2M\right)\right)}{\sqrt{\pi}r(6M + r(pr-2)) - 32\sqrt{\Theta}M} \tag{12}$$

The denominator $2f - rf'$ determines the admissible range of circular motion, while the radial dependence of $f(r)$ encodes the separate contributions of p and Θ. Figures 5 and 6 display the radial profiles of $\mathcal{E}_c$ and $\mathcal{L}_c$. The variation of p changes these profiles through the linear term $-pr$, which grows with radius for $\omega_q = -2/3$ and therefore affects both the near-horizon and the intermediate circular-orbit domains. The noncommutative parameter Θ, entering through $\sqrt{\Theta}/r^2$, mainly modifies the strong-field region close to the compact object. Thus the circular-orbit structure is shaped by two complementary effects: p controls the quintessence-field deformation, whereas Θ controls the short-distance noncommutative correction.

4.2. Innermost stable and innermost bound circular orbits

The ISCO is the marginally stable circular orbit, obtained by imposing the circular-orbit conditions together with $d^2V_{\rm eff}/dr^2 = 0$. Equivalently, for a static, spherically symmetric spacetime the ISCO radius solves [24–26]

$$f(r)f''(r) - 2\left[f'(r)\right]^2 + \frac{3}{r}f(r)f'(r) = 0. \tag{13}$$

The IBCO is the innermost bound circular orbit, with $\mathcal{E}_c = 1$; it marks the threshold between bound and plunging orbits and satisfies $dV_{\rm eff}/dr = 0$ with $V_{\rm eff} = \mathcal{E}^2 = 1$ [12, 24]. For the metric (6) both conditions are transcendental and are solved numerically. Figure 7 shows the dependence of $r_{\rm ISCO}$ on p and Θ. In the adopted parameter range, more negative values of p shift the ISCO inward, while the radius approaches the Schwarzschild value $6M$ as $p \to 0$. Increasing Θ also moves the ISCO inward, mainly through the inner correction $\sqrt{\Theta}/r^2$; compared with the quintessence term, this effect is more localized in the strong-field region.

To reduce the number of free parameters in the periodic-orbit analysis, we follow Refs. [4, 12] and fix the angular momentum at

$$\mathcal{L}_{\rm av} = \frac{\mathcal{L}_{\rm ISCO} + \mathcal{L}_{\rm IBCO}}{2}, \tag{14}$$

so that $\mathcal{L}_{\rm ISCO} < \mathcal{L}_{\rm av} < \mathcal{L}_{\rm IBCO}$. Table 1 lists $r_{\rm ISCO}$, $r_{\rm IBCO}$, $\mathcal{L}_{\rm ISCO}$, $\mathcal{L}_{\rm IBCO}$, and $\mathcal{L}_{\rm av}$ for representative parameter sets. We note an important physical feature of this geometry: because the p term is linear and grows with r for $\omega_q = -2/3$, the bound-orbit region between the ISCO and the IBCO shrinks rapidly as $|p|$ increases, and the IBCO ceases to exist for $p \lesssim -0.02$. The periodic-orbit analysis is therefore restricted to the narrow band

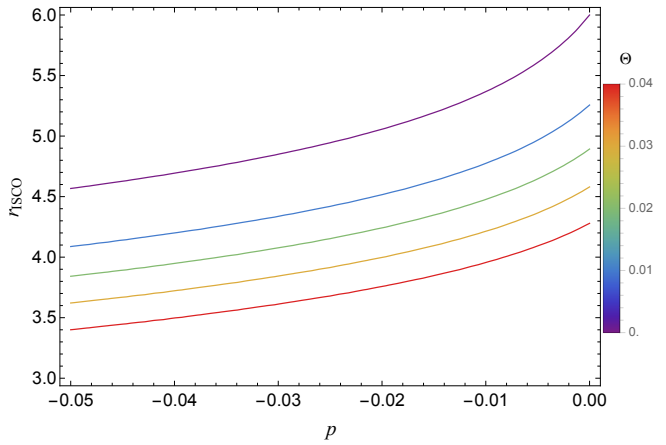


Figure 7: Dependence of the ISCO radius on the quintessence field strength parameter p (left, curves of Θ) and on the noncommutative parameter Θ (right, curves of p).

Table 1: Characteristic radii and angular momenta of circular orbits around the NCiBHSQ. Upper block: fixed $\Theta = 0.01$ with varying p. Lower block: fixed $p = -0.005$ with varying Θ ($\Theta = 0$ corresponds to the quintessence limit). The Schwarzschild values $r_{\rm ISCO} = 6M$, $r_{\rm IBCO} = 4M$ are recovered for $\Theta = p = 0$.

	$r_{\rm ISCO}$	$r_{\rm IBCO}$	$\mathcal{L}_{\rm ISCO}$	$\mathcal{L}_{\rm IBCO}$	$\mathcal{L}_{\rm av}$
			$\Theta = 0.01$		
$p = 0.000$	5.2567	3.5009	3.2252	3.7511	3.4881
$p = -0.002$	5.1229	3.5476	3.2539	3.6984	3.4762
$p = -0.004$	5.0144	3.6033	3.2797	3.6459	3.4628
$p = -0.006$	4.9232	3.6718	3.3032	3.5932	3.4482
$p = -0.008$	4.8445	3.7595	3.3247	3.5401	3.4324
$p = -0.010$	4.7753	3.8798	3.3445	3.4861	3.4153
			$p = -0.005$		
$\Theta = 0.000$	5.6083	4.2139	3.5534	3.8390	3.6962
$\Theta = 0.010$	4.9670	3.6357	3.2917	3.6196	3.4556
$\Theta = 0.020$	4.6471	3.3593	3.1653	3.5105	3.3379
$\Theta = 0.030$	4.3660	3.1206	3.0570	3.4155	3.2362
$\Theta = 0.040$	4.0928	2.8899	2.9548	3.3240	3.1394

of p in which an IBCO exists, which we adopt below. As a consistency check, in the Schwarzschild limit ($\Theta \to 0$, $p \to 0$) we recover $r_{\rm ISCO} = 6M$ and $r_{\rm IBCO} = 4M$.

5. Periodic orbits

We now investigate the periodic orbits of test particles around the NCiBHSQ using Levin's classification scheme [4, 27]. Bound orbits oscillate in both the radial coordinate r and the angular coordinate ϕ. A periodic orbit arises when the ratio of the angular to radial orbital frequencies, $q = \omega_\phi/\omega_r$, is a positive rational number, so that the trajectory closes after a finite interval. The rational number q can be expressed in terms of three integers (z, w, v) as

$$q = w + \frac{v}{z} = \frac{\Delta\phi}{2\pi} - 1, \tag{15}$$

where

$$\Delta\phi = 2\int_{r_-}^{r_+} \frac{\dot{\phi}}{\dot{r}}\, dr = 2\int_{r_-}^{r_+} \frac{\mathcal{L}/r^2}{\sqrt{\mathcal{E}^2 - f(r)\,(1 + \mathcal{L}^2/r^2)}}\, dr. \tag{16}$$

The integer z denotes the number of zooms (leaves), w the number of whirls, and v the number of vertices. The radial motion is bounded between the two turning points r_- and r_+, the periastron and apastron, which are the roots of $\dot{r}^2 = 0$, i.e. $\mathcal{E}^2 = V_{\rm eff}$. Fixing $\mathcal{L} = \mathcal{L}_{\rm av}$, the rational number q in Eqs. (15)–(16) depends only on the orbital energy $\mathcal{E}$, which we invert numerically to obtain the energy of each (z, w, v) orbit.

Tables 2 and 3 list the energies of the $(z, 1, 1)$ periodic orbits for fixed $\Theta = 0.01$ with varying p, and for fixed $p = -0.005$ with varying Θ, respectively. The Schwarzschild values, recovered for $\Theta = p = 0$, agree with those reported in the literature [12]. Table 2 shows that, at fixed Θ, making p more negative raises the energy of the periodic orbits monotonically; the missing $(1, 1, 0)$ entry at $p = -0.010$ reflects the shrinking of the bound-orbit window discussed above. Table 3 shows that, at fixed p, increasing Θ lowers the periodic-orbit energies and shifts $\mathcal{L}_{\rm av}$ to smaller values, consistent with the inward displacement of the characteristic radii.

Table 2: Energy $\mathcal{E}$ and corresponding $\mathcal{L}_{\rm av}$ of periodic orbits $(z, 1, 1)$ around the NCiBHSQ for fixed $\Theta = 0.01$ and various p.

p	$\mathcal{L}_{\rm av}$	$\mathcal{E}_{(1,1,0)}$	$\mathcal{E}_{(2,1,1)}$	$\mathcal{E}_{(3,1,1)}$	$\mathcal{E}_{(4,1,1)}$
0.000	3.4881	0.9608	0.9640	0.9635	0.9631
−0.002	3.4762	0.9675	0.9699	0.9695	0.9692
−0.004	3.4628	0.9733	0.9754	0.9751	0.9748
−0.006	3.4482	0.9787	0.9807	0.9804	0.9801
−0.008	3.4324	0.9838	0.9858	0.9855	0.9852
−0.010	3.4153	–	0.9907	0.9903	0.9901

Table 3: Energy $\mathcal{E}$ and corresponding $\mathcal{L}_{\rm av}$ of periodic orbits $(z, 1, 1)$ around the NCiBHSQ for fixed $p = -0.005$ and various Θ. The first row ($\Theta = 0$) corresponds to the Kiselev limit.

Θ	$\mathcal{L}_{\rm av}$	$\mathcal{E}_{(1,1,0)}$	$\mathcal{E}_{(2,1,1)}$	$\mathcal{E}_{(3,1,1)}$	$\mathcal{E}_{(4,1,1)}$
0.00	3.6962	0.9819	0.9836	0.9833	0.9831
0.01	3.4556	0.9760	0.9781	0.9777	0.9775
0.02	3.3379	0.9726	0.9750	0.9746	0.9743
0.03	3.2362	0.9692	0.9721	0.9716	0.9712
0.04	3.1394	0.9655	0.9690	0.9684	0.9680

Figure 8 illustrates the zoom-whirl periodic orbits of massive particles lying between the ISCO and the IBCO around the NCiBHSQ for $\Theta = 0.01$ and $p = -0.005$, plotted in the Cartesian plane $x = (r/M)\cos\phi$, $y = (r/M)\sin\phi$. The Schwarzschild $(1, 1, 0)$ orbit is shown for comparison in the first panel. Each orbit, identified by its triplet (z, w, v), corresponds to a distinct energy: the number of leaves equals z and the number of central loops reflects the whirl behaviour. The orbits exhibit qualitative similarities to those in Schwarzschild and Kerr spacetimes, but the noncommutative and quintessence corrections compress the

orbits toward the BH and modify their energy profiles, as quantified in Tables 2 and 3.

6. Gravitational wave radiation from periodic orbits

We now study the GW radiation emitted by periodic orbits of a test particle in the NCiBHSQ background. We model the system as an EMRI, in which the orbiting body has mass $m \ll M$ and is treated as a perturbation to the central BH. When the energy $\mathcal{E}$ and angular momentum $\mathcal{L}$ of the particle vary slowly through GW emission, the adiabatic approximation holds and the motion closely follows the periodic orbits over several cycles.

To compute the waveforms we adopt the kludge approach [19], in which the periodic trajectory is obtained by numerically solving the geodesic equations and the GW signal is constructed from the mass-quadrupole formula, valid up to quadratic order [13, 14, 20, 21],

$$h_{ij} = \frac{4\eta M}{D_L}\left(V_i V_j - \frac{m}{r} n_i n_j\right), \tag{17}$$

where $\eta = Mm/(M+m)^2$ is the symmetric mass ratio, D_L is the luminosity distance, V_i are the spatial velocity components of the particle, and n_i is the unit radial vector. Projecting onto the transverse-traceless gauge yields the plus and cross polarizations [12, 20]

$$h_+ = -\frac{2\eta}{D_L}\frac{M^2}{r}\left(1+\cos^2\iota\right)\cos\left(2\phi+2\zeta\right), \tag{18}$$

$$h_\times = -\frac{4\eta}{D_L}\frac{M^2}{r}\cos\iota\,\sin\left(2\phi+2\zeta\right), \tag{19}$$

where ι is the inclination angle between the orbital angular momentum and the line of sight, and ζ is the latitudinal viewing angle. For definiteness we fix $\iota = \zeta = \pi/4$ and $D_L = 200$ Mpc, and we convert the strains to physical units using $M \to GM/c^2$ and 1 Mpc $= 3.085677581 \times 10^{22}$ m, with $G = 6.67430 \times 10^{-11}$ m^3 kg^{-1} s^{-2} and $c = 2.99792458 \times 10^8$ m s^{-1}; the strains are shown normalized by 10^{-21} for a central mass $M = 10^6\,M_\odot$ and companion $m = 10\,M_\odot$.

Figures 9 and 10 show the periodic orbit and the corresponding h_+ and $h_\times$ waveforms for the triplet $(3,1,1)$ at two representative parameter sets, while Fig. 11 overlays the two cases. Figures 12–14 present the analogous results for the triplet $(4,1,1)$. In all cases the waveforms exhibit the characteristic zoom-whirl structure: during the zoom phase the particle moves along an extended, elliptical segment far from the BH, where the gravitational field is weaker, producing the quiet portions of the signal that correspond to the leaves of the orbit. As the particle spirals inward it enters the whirl phase, executing tight, nearly circular loops in the strong-field region, which generate sharp, high-amplitude bursts. The number of quiet intervals equals the number of zoom leaves, while the number of bursts reflects the number of whirls, so that the waveform directly encodes the orbital structure specified by (z, w, v).

Comparing the two parameter sets in Figs. 11 and 14, the combined effect of the noncommutative and quintessence corrections introduces a clear phase shift and a modulation of the amplitude relative to one another. A more compact orbit (larger Θ and more negative p, with smaller apastron) shortens the radial period and increases the burst repetition rate, while the quieter zoom segments are correspondingly compressed. These deviations, although modest, are imprinted directly on the GW phase evolution and constitute observable signatures of the underlying spacetime parameters. For the supermassive-mass scale adopted here, the characteristic frequencies fall in the millihertz band, within the sensitivity range of space-based detectors such as LISA, so that future observations of EMRI waveforms could in principle probe or constrain the noncommutative parameter Θ and the quintessence field strength parameter p.

7. Conclusion

In this work, we investigated the periodic orbits of a massive test particle and the associated gravitational-wave radiation around the NCiBHSQ. The geometry is controlled by two parameters acting in complementary radial domains: the quintessence field strength parameter p, which enters the metric function as a linear term and modifies the intermediate and outer regions, and the noncommutative parameter Θ, which smears the central mass and modifies the strong-field, near-horizon region.

Analyzing the effective potential and the specific energy and angular momentum of circular orbits, we determined the ISCO and IBCO radii and showed that both corrections move the characteristic radii inward relative to the Schwarzschild case, with the standard values $r_{\rm ISCO} = 6M$ and $r_{\rm IBCO} = 4M$ recovered in the appropriate limit. We found an important structural feature of this spacetime: because the Kiselev term grows with radius for $\omega_q = -2/3$, the bound-orbit region between the ISCO and the IBCO contracts rapidly as $|p|$ increases, and the IBCO disappears for $p \lesssim -0.02$. Consequently, bound zoom-whirl periodic orbits exist only within a narrow band of the quintessence parameter, which is itself a constraint that observations of such orbits could test.

We classified the periodic orbits using the zoom-whirl taxonomy and tabulated the energies of the $(z,1,1)$ orbits as functions of p and Θ. A more negative p raises the orbital energies, whereas increasing Θ lowers them and shifts $\mathcal{L}_{\rm av}$ to smaller values. We then computed the plus and cross GW polarizations of representative $(3,1,1)$ and $(4,1,1)$ orbits within the kludge approximation. The waveforms display the characteristic zoom-whirl pattern of quiet zoom segments interrupted by sharp whirl bursts, with the number of leaves and loops directly encoded in the signal. Varying Θ and p introduces a measurable phase shift and amplitude modulation, and shrinks the orbit so that the burst repetition rate increases. For supermassive central masses, these signals fall in the millihertz band accessible to LISA, indicating that future space-based GW observations of EMRIs may provide a route to probing or constraining noncommutative and quintessence corrections to the strong-field geometry.

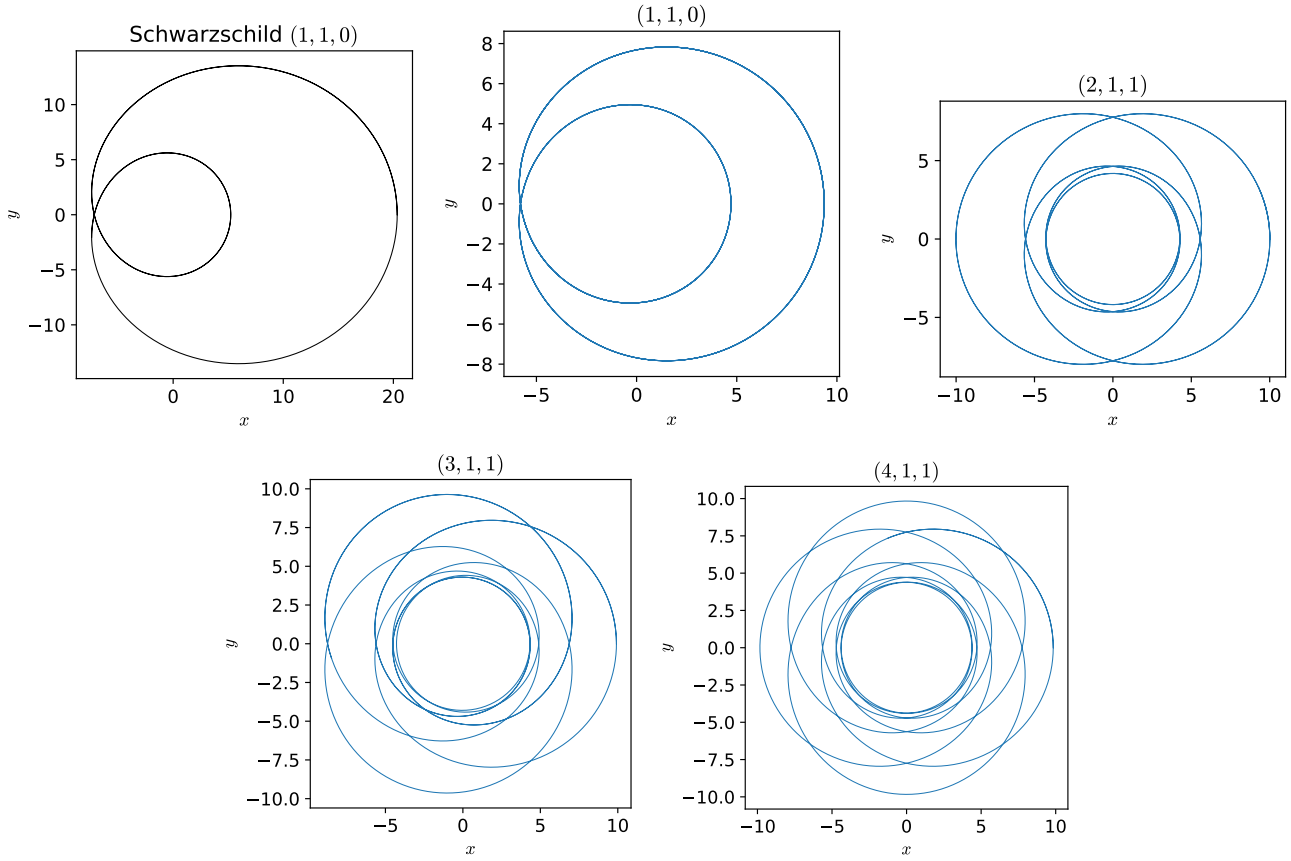


Figure 8: Zoom-whirl periodic orbits for the triplets $(1, 1, 0)$, $(2, 1, 1)$, $(3, 1, 1)$, and $(4, 1, 1)$ around the noncommutative-inspired Kiselev BH with $\Theta = 0.01$ and $p = -0.005$, plotted using $x = (r/M)\cos\phi$, $y = (r/M)\sin\phi$. The first panel shows the Schwarzschild $(1, 1, 0)$ orbit for reference.

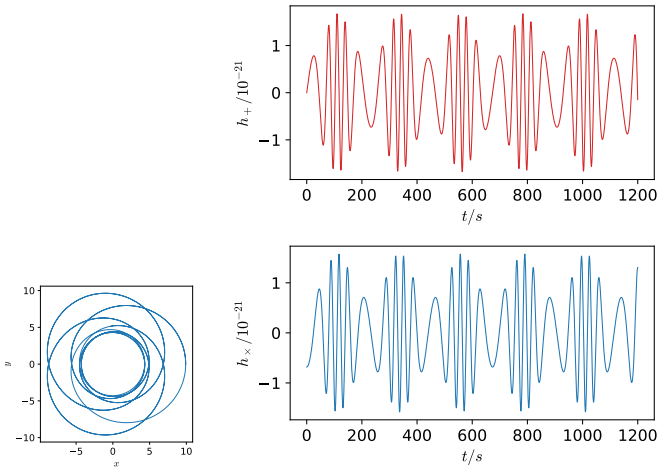


Figure 9: The case $\Theta = 0.01$, $p = -0.005$, $\mathcal{L}_{\rm av} = 3.45564$ and $\mathcal{E} = 0.977744$. The periodic orbit (left) and the GW polarizations h_+ (top right) and $h_\times$ (bottom right) for the triplet $(3, 1, 1)$.

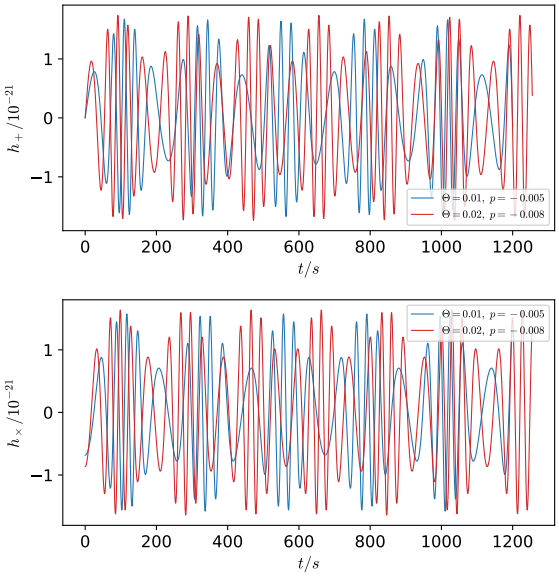


Figure 11: Upper panel: combination of the h_+ waveforms of Figs. 9 and 10. Lower panel: combination of the $h_\times$ waveforms of Figs. 9 and 10, for the triplet $(3, 1, 1)$.

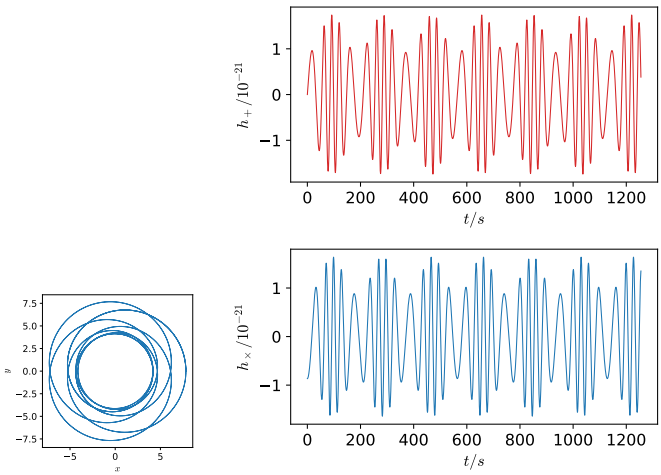


Figure 10: The case $\Theta = 0.02$, $p = -0.008$, $\mathcal{L}_{\rm av} = 3.31648$ and $\mathcal{E} = 0.981955$. The periodic orbit (left) and the GW polarizations h_+ (top right) and $h_\times$ (bottom right) for the triplet $(3, 1, 1)$.

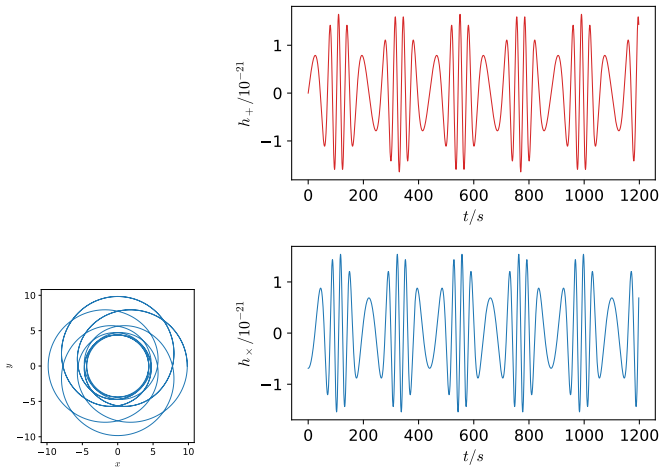


Figure 12: The case $\Theta = 0.01$, $p = -0.005$, $\mathcal{L}_{\rm av} = 3.45564$ and $\mathcal{E} = 0.977487$. The periodic orbit (left) and the GW polarizations h_+ (top right) and $h_\times$ (bottom right) for the triplet $(4, 1, 1)$.

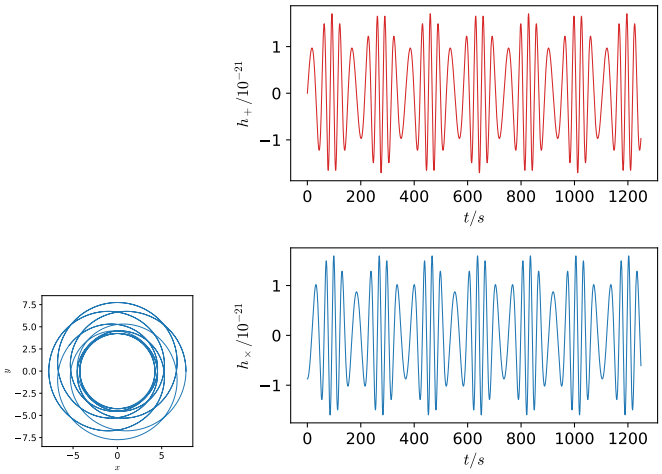


Figure 13: The case $\Theta = 0.02$, $p = -0.008$, $\mathcal{L}_{\rm av} = 3.31648$ and $\mathcal{E} = 0.981657$. The periodic orbit (left) and the GW polarizations h_+ (top right) and $h_\times$ (bottom right) for the triplet (4, 1, 1).

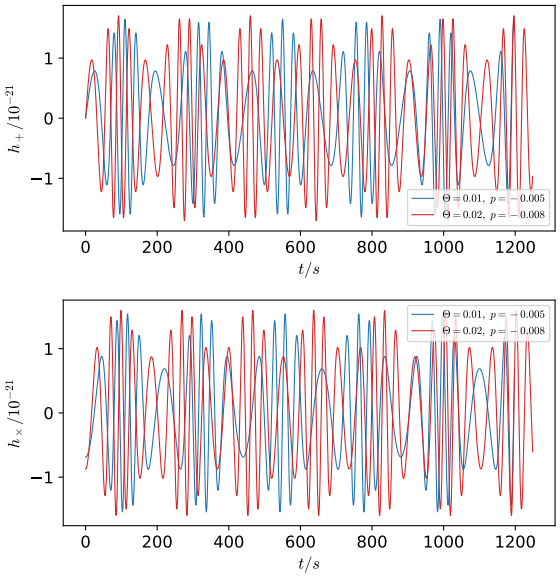


Figure 14: Upper panel: combination of the h_+ waveforms of Figs. 12 and 13. Lower panel: combination of the $h_\times$ waveforms of Figs. 12 and 13, for the triplet (4, 1, 1).

Author contributions

Sh.K. — Theoretical background, manuscript writing
Sh.G. — Literature review, theoretical background
Y.M. — Literature review
J.P. — Figures, code
A.E. — Calculations, code
A.S. — Conceptualization, Manuscript writing

Funding

No funding has been received for this research.

Data availability

All data generated or analysed during this study are included in this published article.

Code Availability

Not applicable.

Declarations

Ethics Approval and Consent to Participate

Not applicable.

Consent for Publication

Not applicable.

Competing Interests

The authors declare no competing interests.

References

[1] B. P. Abbott, R. Abbott, T. D. Abbott, M. R. Abernathy, F. Acernese, K. Ackley, C. Adams, T. Adams, P. Addesso, R. X. Adhikari, and et al., Physical Review Letters **116**, 061102 (2016), arXiv:1602.03837 [gr-qc] .

[2] B. P. Abbott *et al.* (LIGO Scientific, Virgo), Phys. Rev. Lett. **116**, 061102 (2016), arXiv:1602.03837 [gr-qc] .

[3] D. Psaltis, Gen. Rel. Grav. **51**, 137 (2019).

[4] J. Levin and G. Perez-Giz, Physical Review D **77**, 103005 (2008).

[5] X.-M. Deng, Phys. Dark Univ. **30**, 100629 (2020).

[6] K. Glampedakis, Classical and Quantum Gravity **22**, S605 (2005).

[7] S. Babak, H. Fang, J. R. Gair, K. Glampedakis, and S. A. Hughes, Phys. Rev. D **75**, 024005 (2007), [Erratum: Phys.Rev.D 77, 04990 (2008)], arXiv:gr-qc/0607007 .

[8] S. Yang, Y.-P. Zhang, T. Zhu, L. Zhao, and Y.-X. Liu, JCAP **01**, 091 (2025), arXiv:2407.00283 [gr-qc] .

[9] J. Levin and R. Grossman, Phys. Rev. D **79**, 043016 (2009).

[10] R. Grossman and J. Levin, Phys. Rev. D **79**, 043017 (2009).

[11] G. Z. Babar, A. Z. Babar, and Y.-K. Lim, Physical Review D **96**, 084052 (2017).

[12] O. Shabbir, M. Jamil, and M. Azreg-Aïnou, Physics of the Dark Universe **47**, 101816 (2025).

[13] Z.-Y. Tu, T. Zhu, and A. Wang, Physical Review D **108**, 024035 (2023).

[14] S. Yang, Y.-P. Zhang, T. Zhu, L. Zhao, and Y.-X. Liu, arXiv preprint arXiv:2407.00283 (2024).

[15] K. V., Class. Quantum Gravity **20**, 1187 (2003).

[16] P. Nicolini, A. Smailagic, and E. Spallucci, Physics Letters B **632**, 547 (2006), arXiv:gr-qc/0510112 [gr-qc] .

[17] P. Nicolini, International Journal of Modern Physics A **24**, 1229 (2009), arXiv:0807.1939 [hep-th] .

[18] Y.-G. Miao, Z. Xue, and S.-J. Zhang, General Relativity and Gravitation **44**, 555 (2012), arXiv:1012.2426 [hep-th] .

[19] S. Babak, H. Fang, J. R. Gair, K. Glampedakis, and S. A. Hughes, Physical Review D **75**, 024005 (2007).

[20] A. Maselli, N. Franchini, L. Gualtieri, T. P. Sotiriou, S. Barsanti, and P. Pani, Nature Astronomy **6**, 464 (2022).

[21] D. Liang, R. Xu, Z.-F. Mai, and L. Shao, Physical Review D **107**, 044053 (2023).

[22] M. P. Hobson, G. P. Efstathiou, and A. N. Lasenby, *General Relativity: An Introduction for Physicists* ((Cambridge University Press, 2006)).

[23] H. Goldstein, *Classical Mechanics* ((Pearson Education India, 2011)).

[24] C. Bambi, *Black Holes: A Laboratory for Testing Strong Gravity* (Springer Singapore, Singapore, 2017).

[25] B. Gao and X.-M. Deng, Annals of Physics **418**, 168194 (2020).

[26] T. Zahra, M. Jamil, and M. Azreg-Aïnou, Nucl. Phys. B **1017**, 116954 (2025), arXiv:2505.06443 [gr-qc] .

[27] J. Levin, Classical and Quantum Gravity **26**, 235010 (2009).